Robust Statistics for Multi-Band SAR Image Change Detection

Moustapha Diaw*, Olivier Lerda†, Joana Frontera-Pons*, Frédéric Brigui*, Jean-Philippe Ovarlez*‡
*DEMR, ONERA, University Paris Saclay, †Exail Sonar Systems division,
‡SONDRA, CentraleSupélec, University Paris Saclay

***Abstract*—Change detection remains a classic but essential problem in Synthetic Aperture Radar (SAR) imagery. When designing statistical change detection schemes, SAR data are typically modeled as Gaussian random vectors, and the corresponding tests have been designed using Gaussian distributions. Considering the heterogeneous nature of SAR images, SAR data were then extended to a mixture of scaled Gaussian distributions where the unknown scaling parameter (usually called texture) acts in the model on the whole information vector. This paper proposes to extend the conventional model by designing a new robust detector based on the Generalized Likelihood Ratio Test (GLRT) technique for multi-band change detection. In our model, different textures are considered to characterize the different bands. The Constant False Alarm Rate (CFAR) behavior has been analyzed, and simulation and experimental SAR data show promising results.**

***Index Terms*—Change Detection, GLRT, Mixture of Scaled Gaussian Distributions, Robust Estimation, SAR Imaging**

I. Introduction

In the last few years, change detection using SAR imagery has developed considerably with the availability of Earth satellite imagery from Sentinel-1, TerraSAR-X, etc., and the proliferation of related applications such as structure monitoring, forest, glacier, and soil classification, among others. The considerable progress in terms of resolution of the new imaging systems and the significant contribution of diversity (polarimetric, temporal, spectral, azimuthal) require the development of new processing tools. Traditional techniques for detecting coherent changes are based solely on the comparison of empirical covariance matrices (Sample Covariance Matrix) associated to the Gaussian hypothesis of SAR signals [1], [2]. A complete review of these classical detectors can be found in [3].

Complex Elliptically Symmetric (CES) distributions have recently been investigated for clutter modeling [4], [5]. They account for the non-Gaussianity and heterogeneity of the SAR data, providing a heavy-tailed alternative to the multivariate Normal model. They allow, for example, to model the clutter power through a random (CES) or deterministic (mixture of scaled-Gaussian distributions) scalar variable called the texture [6], [7].

We propose in this paper to extend the model introduced in [6] to multi-band SAR change detection. In [6], the texture is considered the same on the signal vector. So when additional diversity, such as multiple frequency bands, is available, this model is no longer accurate. The method proposed in this paper assumes different textures for characterizing each band. This approach has already been studied in [8] for concatenating two signal returns from two collocated antennas for Sonar target detection. Here, we propose using this methodology to develop a new GLRT for change detection based on the texture and the covariance matrix equality.

The rest of the article is organized as follows: Section II presents the general model and the theoretical solution to this problem (GLRT solution) with some extended proofs in Appendix. Section III illustrates the performance of the proposed method on Monte-Carlo trials and a SAR experimental dataset.

Notations: Italic type indicates a scalar quantity, lower case boldface indicates a vector quantity, and upper case boldface indicates a matrix. The transpose conjugate operator is ^{H}. $tr\{\cdot\}$ and $|\cdot|$ are respectively the trace and the determinant operators. $\mathbf{x} \sim \mathcal{CN}(\boldsymbol{\mu}, \boldsymbol{\Sigma})$ is a complex-valued circular random Normal vector of mean $\boldsymbol{\mu}$ and covariance matrix $\boldsymbol{\Sigma}$. $\mathbf{I}_p$ and $\mathbf{0}_p$ are the identity matrix and the null matrix of size $p \times p$, respectively.

II. Derivation of the GLRT

This section first describes the model used to represent the random vectors of multi-band SAR images, followed by the derivation of our GLRT from a binary hypothesis test.

A. Model

Let us consider $\mathbf{x}_1, \mathbf{x}_2, \ldots, \mathbf{x}_m$ pixels from the m frequency bands ($m \geq 1$) in polarimetric SAR images. Each pixel $\mathbf{x}_i$ is a p-vector (p polarizations) distributed according to $\mathcal{CN}(\mathbf{0}, \tau_i \boldsymbol{\Phi}_i)$ where the deterministic scalars $\{\tau_i\}_{i\in[1,m]} \in \mathbb{R}^+$ and the matrices $\{\boldsymbol{\Phi}_i\}_{i\in[1,m]} \in \mathbb{S}_p^H$ (set of Hermitian semi-definite matrices of size $p\times p$) represent the unknown textures and covariance matrices for each band, respectively. Such a model is referred to as a mixture of scaled Gaussian distributions [9]. In this paper, we stack, for a given pixel location, the different frequency bands such that $\mathbf{x} = \left[\mathbf{x}_1^T, \mathbf{x}_2^T, \ldots, \mathbf{x}_m^T\right]^T$. The vector $\mathbf{x} \in \mathbb{C}^{mp}$ is then distributed as $\mathcal{CN}(\mathbf{0}, \boldsymbol{\Sigma})$:

$$p_{\mathbf{x}}(\mathbf{x}, \boldsymbol{\Sigma}) = \frac{1}{\pi^{m\,p}\,|\boldsymbol{\Sigma}|} \exp\left(-\mathbf{x}^H\,\boldsymbol{\Sigma}^{-1}\,\mathbf{x}\right), \tag{1}$$

where the covariance matrix $\boldsymbol{\Sigma} = E(\mathbf{x}\,\mathbf{x}^H)$ can be put in the compact form: $\boldsymbol{\Sigma} = \mathbf{T}\,\boldsymbol{\Phi}\,\mathbf{T}$, where the matrix $\boldsymbol{\Phi}$ and $\mathbf{T}$ are

defined as:

$$\mathbf{\Phi} = \begin{pmatrix} \mathbf{\Phi}_1 & E\left(\mathbf{x}_1\mathbf{x}_2^H\right) & \dots & E\left(\mathbf{x}_1\mathbf{x}_m^H\right) \\ E\left(\mathbf{x}_2\mathbf{x}_1^H\right) & \mathbf{\Phi}_2 & \dots & E\left(\mathbf{x}_2\mathbf{x}_m^H\right) \\ \vdots & \vdots & \ddots & \vdots \\ E\left(\mathbf{x}_m\mathbf{x}_1^H\right) & E\left(\mathbf{x}_m\mathbf{x}_2^H\right) & \dots & \mathbf{\Phi}_m \end{pmatrix},$$

$$\mathbf{T} = \begin{pmatrix} \sqrt{\tau_1}\,\mathbf{I}_p & \mathbf{0}_p & \dots & \mathbf{0}_p \\ \mathbf{0}_p & \sqrt{\tau_2}\,\mathbf{I}_p & \dots & \mathbf{0}_p \\ \vdots & \vdots & \ddots & \vdots \\ \mathbf{0}_p & \mathbf{0}_p & \dots & \sqrt{\tau_m}\,\mathbf{I}_p \end{pmatrix}.$$

B. Hypothesis test and derivation of GLRT

1) Hypothesis test: For each pixel under test, the change detection problem in SAR images acquired at two dates $t = 1$ and $t = 2$ can be formulated as:

$$\begin{cases} H_0 : \boldsymbol{\theta}_1 = \boldsymbol{\theta}_2 \\ H_1 : \boldsymbol{\theta}_1 \neq \boldsymbol{\theta}_2 \end{cases} \tag{2}$$

with $\forall t \in \{1,2\}$, $\boldsymbol{\theta}_t = \{\mathbf{T}_t, \mathbf{\Phi}_t\}$. Under H_0, we note that $\boldsymbol{\theta}_1 = \boldsymbol{\theta}_2 = \boldsymbol{\theta} = \{\mathbf{T}, \mathbf{\Phi}\}$. Under H_1, we note $\boldsymbol{\theta}_t = \{\mathbf{T}_t, \mathbf{\Phi}_t\}$. For the two SAR images 1 and 2, we can define a spatial boxcar centered around each pixel $\mathbf{x}$ under test with N secondary data and note these secondary data as $\{\mathbf{x}_k^t\}_{k\in[1,N]}$ for the image at date t.

2) Derivation of the GLRT: The detector can be derived using the Maximum Likelihood procedure when the texture and covariance matrices are unknown:

$$\Lambda_B(\mathbf{x}) = \frac{\boldsymbol{\mathcal{L}}_1\left(\left\{\left\{\mathbf{x}_k^t, \mathbf{T}_k^t\right\}_{k\in[1,N]}, \mathbf{\Phi}_t\right\}_{t\in[1,2]}\right)}{\boldsymbol{\mathcal{L}}_0\left(\left\{\left\{\mathbf{x}_k^t\right\}_{k\in[1,N]}\right\}_{t\in[1,2]}, \{\mathbf{T}_k\}_{k\in[1,N]}, \mathbf{\Phi}\right)}, \tag{3}$$

where

$$\boldsymbol{\mathcal{L}}_1\left(\left\{\left\{\mathbf{x}_k^t, \mathbf{T}_k^t\right\}_k, \mathbf{\Phi}_t\right\}_t\right) = \prod_{\substack{k=1\\t=1}}^{\substack{k=N\\t=2}} p_{\mathbf{x}}\left(\mathbf{x}_k^t, \mathbf{T}_k^t\,\mathbf{\Phi}_t\,\mathbf{T}_k^t\right), \tag{4}$$

and

$$\boldsymbol{\mathcal{L}}_0\left(\left\{\left\{\mathbf{x}_k^t\right\}_k\right\}_t, \{\mathbf{T}_k\}_k, \mathbf{\Phi}\right) = \prod_{\substack{k=1\\t=1}}^{\substack{k=N\\t=2}} p_{\mathbf{x}}\left(\mathbf{x}_k^t, \mathbf{T}_k\,\mathbf{\Phi}\,\mathbf{T}_k\right). \tag{5}$$

This likelihood function is then maximized with respect to the unknown parameters.

Proposition 2.1: the GLRT under the binary hypothesis test presented in (2) can be expressed as follows:

$$\hat{\Lambda}_B(\mathbf{x}) = \frac{\left|\hat{\mathbf{\Phi}}\right|^{2N}}{\prod_{t=1}^{2}\left|\hat{\mathbf{\Phi}}_t\right|^{N}} \prod_{k=1}^{N} \frac{\left|\hat{\mathbf{T}}_k\right|^4}{\prod_{t=1}^{2}\left|\hat{\mathbf{T}}_k^t\right|^2} \underset{H_0}{\overset{H_1}{\gtrless}} \lambda, \tag{6}$$

where λ is the detection threshold and where the unknown parameters $\hat{\mathbf{\Phi}}$, $\left\{\hat{\mathbf{T}}_k\right\}_{k\in[1,N]}$, $\left\{\hat{\mathbf{T}}_k^t\right\}_{k\in[1,N],t\in\{1,2\}}$ and $\left\{\hat{\mathbf{\Phi}}_t\right\}_{t\in\{1,2\}}$ are given, under each hypothesis, by the following joint fixed point equations:

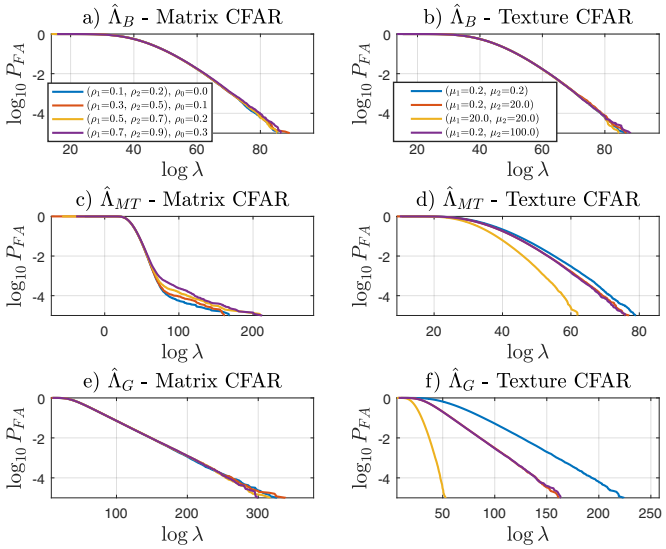

Fig. 1. Matrix and Texture CFARness, P_{FA} vs λ with $N = 16$. a) and b): Proposed method. c) and d): Method proposed in [6]. e) and f): Method proposed in [1].

- under H_0,

$$\begin{cases} \hat{\mathbf{T}}_k = \dfrac{1}{2}\displaystyle\sum_{\substack{t=1\\k=N}}^{\substack{2\\t=2}} \mathrm{Re}\left(\hat{\mathbf{\Phi}}^{-1}\hat{\mathbf{T}}_k^{-1}\,\mathbf{x}_k^t\,\mathbf{x}_k^{tH}\right), \quad \forall k \in [1,N], \\ \hat{\mathbf{\Phi}} = \dfrac{1}{2N}\displaystyle\sum_{\substack{k=1\\t=1}}^{\substack{k=N\\t=2}} \hat{\mathbf{T}}_k^{-1}\,\mathbf{x}_k^t\,\mathbf{x}_k^{tH}\,\hat{\mathbf{T}}_k^{-1}. \end{cases} \tag{7}$$

- under H_1,

$$\begin{cases} \hat{\mathbf{T}}_k^t = \mathrm{Re}\left(\hat{\mathbf{\Phi}}_t^{-1}\left(\hat{\mathbf{T}}_k^t\right)^{-1}\mathbf{x}_k^t\,\mathbf{x}_k^{tH}\right), \forall k \in [1,N], \forall t \in \{1,2\} \\ \hat{\mathbf{\Phi}}_t = \dfrac{1}{N}\displaystyle\sum_{k=1}^{N}\left(\hat{\mathbf{T}}_k^t\right)^{-1}\mathbf{x}_k^t\,\mathbf{x}_k^{tH}\left(\hat{\mathbf{T}}_k^t\right)^{-1}, \quad \forall t \in \{1,2\} \end{cases} \tag{8}$$

Proof: Please see Appendix. ∎

The joint fixed point equations (7) and (8) are solved by recursive iterations

$$\begin{cases} \left(\hat{\mathbf{\Phi}}\right)_{n+1} = f_1\left(\left(\hat{\mathbf{\Phi}}\right)_n, \left(\hat{\mathbf{T}}_k\right)_n\right), \\ \left(\hat{\mathbf{T}}_k\right)_{n+1} = f_2\left(\left(\hat{\mathbf{\Phi}}\right)_n, \left(\hat{\mathbf{T}}_k\right)_n\right), \end{cases}$$

and $\begin{cases} \left(\hat{\mathbf{\Phi}}_t\right)_{n+1} = f_3\left(\left(\hat{\mathbf{\Phi}}_t\right)_n, \left(\hat{\mathbf{T}}_k^t\right)_n\right), \\ \left(\hat{\mathbf{T}}_k^t\right)_{n+1} = f_4\left(\left(\hat{\mathbf{\Phi}}_t\right)_n, \left(\hat{\mathbf{T}}_k^t\right)_n\right), \end{cases}$ with starting points $\left(\hat{\mathbf{\Phi}}_t\right)_0 = \left(\hat{\mathbf{\Phi}}\right)_0 = \mathbf{I}_{mp}$ and $\left(\hat{\mathbf{T}}_k^t\right)_0 = \left(\hat{\mathbf{T}}_k\right)_0 = \mathbf{I}_{mp}$. The functions f_1 to f_4 are given in (7) and (8). The convergence is here reached only for the matrices $\hat{\mathbf{\Phi}}$ and $\hat{\mathbf{\Phi}}_t$.

For only $m = 2$, an analytical expression for the textures $\hat{\mathbf{T}}_k$ and $\hat{\mathbf{T}}_k^t$ can be derived in the same way as in [8] for target detection. For identifiability purpose, a normalization constraint $\mathrm{tr}\left(\hat{\mathbf{\Phi}}\right) = mp$ is imposed on $\hat{\mathbf{\Phi}}$.

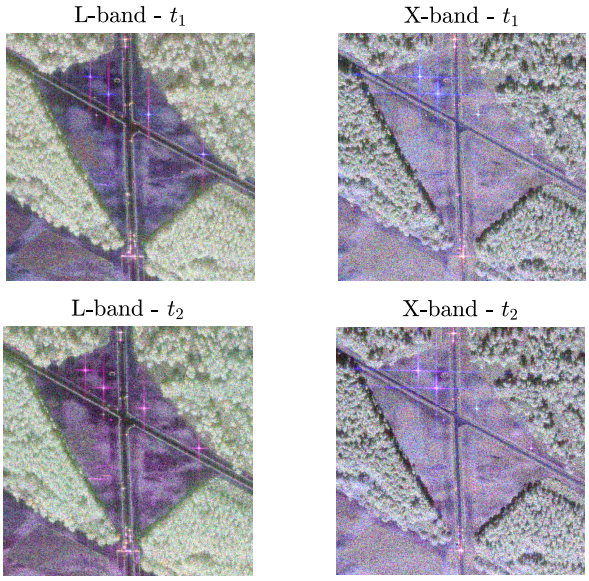

Fig. 2. L and X band SETHI intensity polarimetric SAR images in Pauli basis in RGB color composition (red for $HH-VV$, green for $(HV+VH)/\sqrt{2}$ and blue for $HH+VV$ for two different date t_1 and t_2.

III. Results

In this section, we present the results obtained by our detector compared to the state-of-the-art approaches on both simulations and real data.

A. Results on simulations

In this section, the CFARness behavior of our detector and the one proposed in [6] has been studied for Monte-Carlo simulations when two frequency bands are concatenated. We generate two textured Gaussian random vectors, where the textures are Γ-distributed according to $\Gamma(\mu, 1/\mu)$ distribution within each band at times $t=1$ and $t=2$, we note μ_1 and μ_2 each parameter respectively. The CFAR property is analyzed under H_0, that is when the covariance and texture matrices are equal at times $t=1$ and $t=2$. The covariance matrices chosen in this paper are Toeplitz structured with the form $\mathbf{\Phi}_1 = \left\{\rho_1^{|i-j|}\right\}_{1\leq i,j\leq p}$ for the first band and $\mathbf{\Phi}_2 = \left\{\rho_2^{|i-j|}\right\}_{1\leq i,j\leq p}$ for second band. We have modeled inter-band correlation through $\rho_0 \times \mathbf{1}_p$ where ρ_0 is a fixed degree of inter-band cross-correlation factor to ensure the invertibility of the full-band covariance matrix $\mathbf{\Sigma}$. We investigate the CFAR behavior of the proposed GLRT detector (6) and the $\hat{\Lambda}_{MT}$ detector proposed in [6]-Prop. IV.1 when the two bands are concatenated (and the same texture acting over the two bands). Figure 1 shows the P_{FA} vs threshold λ relationships, obtained through 5×10^5 Monte-Carlo trials with different matrix and texture parameters. We can observe, in a) that the proposed detector (6) and $\hat{\Lambda}_G$ are CFAR-matrix while the detector $\hat{\Lambda}_{MT}$, in c), is not. Unlike our detector, which provides good Pfa regulation, figures 1-d) and f) show a poor false alarm regulation for the $\hat{\Lambda}_{MT}$ detector and the conventional Gaussian detector $\hat{\Lambda}_G$ [1], [10] built with the Sample Covariance Matrix estimate. Moreover, curves a) and b) relative to matrix and texture CFAR look the same and span the same support, meaning that (6) fully adheres to the CFAR property regarding textures and covariance matrices.

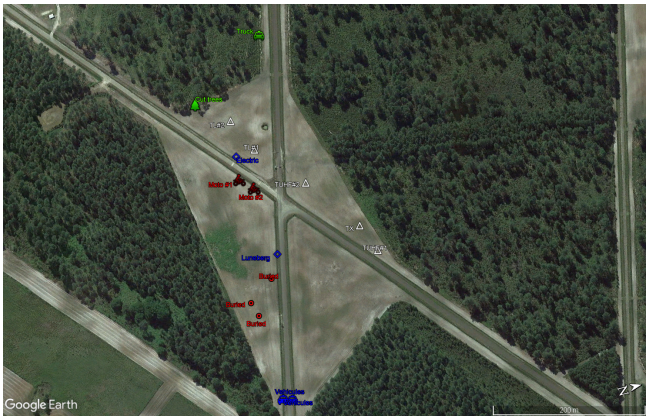

Fig. 3. Ground truth of the studied scene.

B. Results on real data

We illustrate in this section preliminary results obtained on real data. Figure 2 presents the polarimetric SAR dataset evaluated in this section. The SAR images were acquired over an area in the south of France in July 2021 by the ONERA SETHI system [11]. The dataset is composed of images two bands (L and X) and at two different dates t_1 and t_2.

The ground truth is described in Figure 3. Objects in white colors are calibration instruments and remain unchanged between the two acquisitions. Objects in blue colors (except for a few cars at the bottom that moved) remain unchanged, too. Objects in green and red are changes that occur between the two acquisitions.

Figures 4 and 5 show the results of the detectors $\hat{\Lambda}_{MT}$ and $\hat{\Lambda}_G$ proposed respectively in [6] and [1] between t_1 and t_2 for $P_{fa}=10^{-2}$ and $P_{fa}=10^{-3}$ for the mono bands X and L. Both detectors detect the changes of the moved cars (at the bottom) on both frequency bands X and L. Motorcyclists, in the middle, are also detectable on the L frequency band. Figures 6 and 7 present the results of the $\hat{\Lambda}_B$ detector proposed in (6) and the two state-of-the-art detectors proposed in [6] and [1] between t_1 and t_2 for $Pfa=10^{-2}$ and $P_{fa}=10^{-3}$ for the combination of frequency bands (X-L). Preliminary results suggest encouraging performances of our approach. Further work is needed to fully assess the performance on real data.

IV. Conclusion

In this paper, we have developed a new change detection scheme considering the concatenation of fully polarimetric SAR images from different center frequency bands modeled by a scaled Gaussian mixture with different textures. Analysis of the false alarm regulation of the GLRT test shows that the CFAR property is verified concerning the covariance matrix and the texture. This new Multi-band polarimetric SAR change detection scheme has been applied to experimental data.

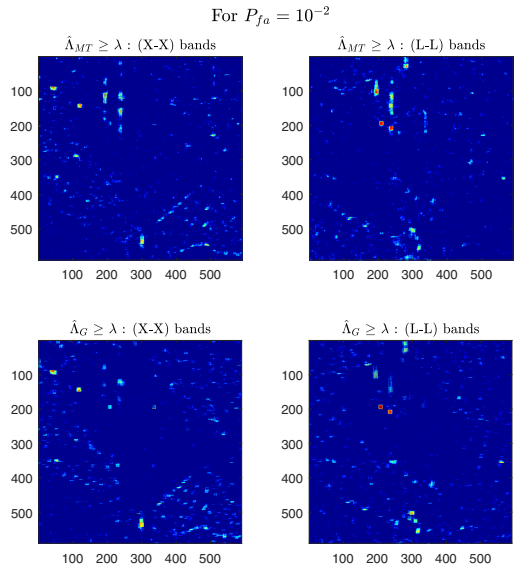

Fig. 4. Detected changes in the X and L bands for the tests $\hat{\Lambda}_{MT}$ and $\hat{\Lambda}_{G}$ proposed in [6] and [1], respectively. Here, we choose $P_{fa} = 10^{-2}$.

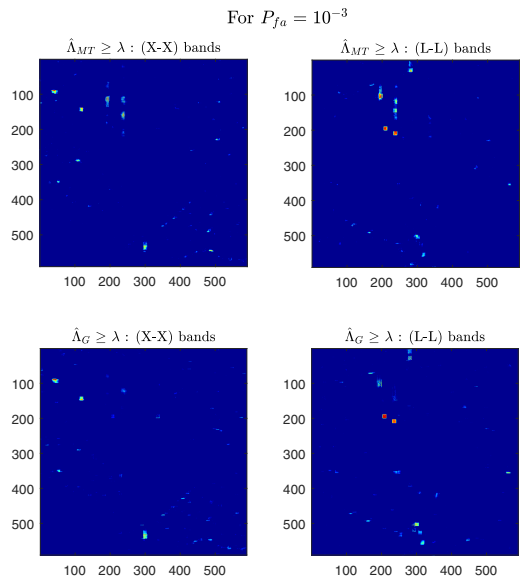

Fig. 5. Detected changes in the X and L bands for the tests $\hat{\Lambda}_{MT}$ and $\hat{\Lambda}_{G}$ proposed in [6] and [1], respectively. Here, we choose $P_{fa} = 10^{-3}$.

APPENDIX: DERIVATION OF THE GLRT

The GLRT can be defined by the optimization of (3) with respect to the unknown parameters. To maximize the two likelihoods $\boldsymbol{\mathcal{L}}_0$ and $\boldsymbol{\mathcal{L}}_1$ defined in (5) and (4) respectively, we have to deal with the following operations:

$$\left(\left\{\hat{\mathbf{T}}_k\right\}_k, \hat{\boldsymbol{\Phi}}\right) = \underset{\left(\{\mathbf{T}_k\}_k, \boldsymbol{\Phi}\right)}{\arg\max}\ \boldsymbol{\mathcal{L}}_0\left(\left\{\left\{\mathbf{x}_k^t\right\}_k\right\}_t, \{\mathbf{T}_k\}_k, \boldsymbol{\Phi}\right),$$

$$\left(\left\{\left\{\hat{\mathbf{T}}_k^t\right\}_k, \hat{\boldsymbol{\Phi}}_t\right\}_t\right) = \underset{\left(\left\{\left\{\mathbf{T}_k^t\right\}_k, \boldsymbol{\Phi}_t\right\}_t\right)}{\arg\max}\ \boldsymbol{\mathcal{L}}_1\left(\left\{\left\{\mathbf{x}_k^t, \mathbf{T}_k^t\right\}_k, \boldsymbol{\Phi}_t\right\}_t\right),$$

where $\left(\left\{\hat{\mathbf{T}}_k\right\}_k, \hat{\boldsymbol{\Phi}}\right)$ are the estimated parameters under H_0 and $\left(\left\{\left\{\hat{\mathbf{T}}_k^t\right\}_k, \hat{\boldsymbol{\Phi}}_t\right\}_t\right)$ are those under H_1. Under each hypothesis, each parameter will be estimated separately assuming the other remaining constant, reintroducing the estimated parameters as necessary.

By denoting $C = -2\,m\,p\,N\,\log(\pi)$, the logarithm of (5), under H_0, is given by:

$$\log(\boldsymbol{\mathcal{L}}_0) = C - \sum_{\substack{k=1\\t=1}}^{\substack{k=N\\t=2}} \log\left(|\boldsymbol{\Phi}|\right) + 2\sum_{\substack{k=1\\t=1}}^{\substack{k=N\\t=2}} \log\left(\left|\mathbf{T}_k^{-1}\right|\right) - \sum_{\substack{k=1\\t=1}}^{\substack{k=N\\t=2}} \left(\mathbf{x}_k^{tH}\,\mathbf{T}_k^{-1}\boldsymbol{\Phi}^{-1}\mathbf{T}_k^{-1}\,\mathbf{x}_k^t\right). \quad (9)$$

Now, we proceed by taking the derivative with respect to $\mathbf{T}_k^{-1}$. Then, $\forall k \in [1, N]$,

$$\frac{\partial \log(\boldsymbol{\mathcal{L}}_0)}{\partial \mathbf{T}_k^{-1}} = 4\sum_{k=1}^{k=N} \mathbf{T}_k - 2\sum_{\substack{k=1\\t=1}}^{\substack{k=N\\t=2}} \mathrm{Re}\left((\boldsymbol{\Phi}\mathbf{T}_k)^{-1}\mathbf{x}_k^t\mathbf{x}_k^{tH}\right) = \mathbf{0}_{m\,p}\,.$$

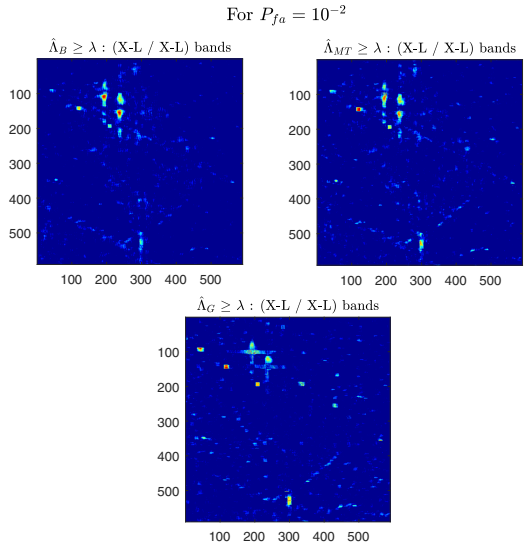

Fig. 6. Detected changes for $P_{fa} = 10^{-2}$ in the concatenated (X-L) bands for $\hat{\Lambda}_{B}$ and the tests $\hat{\Lambda}_{MT}$ and $\hat{\Lambda}_{G}$ proposed in [6] and [1], respectively.

As $\dfrac{\partial \log\left(\left|\mathbf{T}_k^{-1}\right|\right)}{\partial \mathbf{T}_k^{-1}} = \mathbf{T}_k$ and $\mathbf{x}_k^{tH}\left(\mathbf{T}_k\boldsymbol{\Phi}\mathbf{T}_k\right)^{-1}\mathbf{x}_k^t$ is a positive real scalar, then,

$$\mathbf{x}_k^{tH}\left(\mathbf{T}_k\boldsymbol{\Phi}\mathbf{T}_k\right)^{-1}\mathbf{x}_k^t = \mathrm{Re}\left(\mathrm{tr}\left(\mathbf{T}_k^{-1}\boldsymbol{\Phi}^{-1}\mathbf{T}_k^{-1}\,\mathbf{x}_k^t\,\mathbf{x}_k^{tH}\right)\right).$$

Referring to Eq. (117) in [12], we obtain,

$$\frac{\partial \mathrm{tr}\left(\mathbf{T}_k^{-1}\boldsymbol{\Phi}^{-1}\mathbf{T}_k^{-1}\,\mathbf{x}_k^t\,\mathbf{x}_k^{tH}\right)}{\partial \mathbf{T}_k^{-1}} = 2\,\mathrm{Re}\left(\boldsymbol{\Phi}^{-1}\,\mathbf{T}_k^{-1}\,\mathbf{x}_k^t\,\mathbf{x}_k^{tH}\right).$$

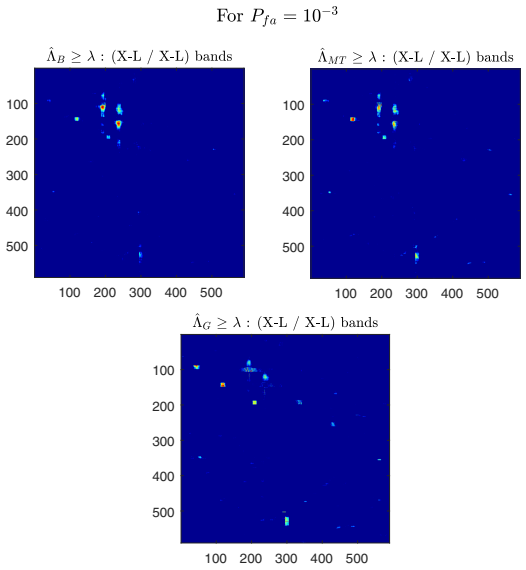

Fig. 7. Detected changes for $P_{fa} = 10^{-3}$ in the concatenated (X-L) bands for $\hat{\Lambda}_B$ and the tests $\hat{\Lambda}_{MT}$ and $\hat{\Lambda}_G$ proposed in [6] and [1], respectively.

Optimizing each $\hat{\mathbf{T}}_k$ individually results in:

$$\forall k \in [1, N], \hat{\mathbf{T}}_k = \frac{1}{2} \sum_{t=1}^{t=2} \mathrm{Re}\left(\mathbf{\Phi}^{-1} \hat{\mathbf{T}}_k^{-1} \mathbf{x}_k^t \mathbf{x}_k^{tH}\right).$$

Let us estimate $\mathbf{\Phi}$ by deriving $\log(\boldsymbol{\mathcal{L}}_0)$ with respect to $\mathbf{\Phi}^{-1}$. This involves by deriving the trace of $(\mathbf{x}_k^{tH} \mathbf{T}_k^{-1}) \mathbf{\Phi}^{-1} (\mathbf{T}_k^{-1} \mathbf{x}_k^t)$ with respect to $\mathbf{\Phi}^{-1}$ (see Eq. (101) in [12]):

$$\frac{\partial \log(\boldsymbol{\mathcal{L}}_0)}{\partial \mathbf{\Phi}^{-1}} = 2N\mathbf{\Phi} - \sum_{\substack{k=1 \\ t=1}}^{\substack{k=N \\ t=2}} \mathbf{T}_k^{-1} \mathbf{x}_k^t \mathbf{x}_k^{tH} \mathbf{T}_k^{-1} = \mathbf{0}_{m\,p}\,.$$

We finally obtain: $\hat{\mathbf{\Phi}} = \frac{1}{2N} \sum_{\substack{k=1 \\ t=1}}^{\substack{k=N \\ t=2}} \hat{\mathbf{T}}_k^{-1} \mathbf{x}_k^t \mathbf{x}_k^{tH} \hat{\mathbf{T}}_k^{-1}$.

The same approach is used for H_1: the texture parameters and the covariance parameter are optimized separately:

$$\log(\boldsymbol{\mathcal{L}}_1) = C - \sum_{\substack{k=1 \\ t=1}}^{\substack{k=N \\ t=2}} \log\left(|\mathbf{\Phi}_t|\right) + 2 \sum_{\substack{k=1 \\ t=1}}^{\substack{k=N \\ t=2}} \log\left(\left|\left(\mathbf{T}_k^t\right)^{-1}\right|\right) - \sum_{\substack{k=1 \\ t=1}}^{\substack{k=N \\ t=2}} \left(\mathbf{x}_k^{tH} \left(\mathbf{T}_k^t\right)^{-1} \mathbf{\Phi}_t^{-1} \left(\mathbf{T}_k^t\right)^{-1} \mathbf{x}_k^t\right). \quad (10)$$

Similarly to H_0, let us derive $\log(\boldsymbol{\mathcal{L}}_1)$ with respect to $\left(\mathbf{T}_k^t\right)^{-1}$ and $\mathbf{\Phi}_t^{-1}$:

$$\frac{\partial \log(\boldsymbol{\mathcal{L}}_1)}{\partial \left(\mathbf{T}_k^t\right)^{-1}} = 2 \sum_{\substack{k=1 \\ t=1}}^{\substack{k=N \\ t=2}} \mathbf{T}_k^t - 2 \sum_{\substack{k=1 \\ t=1}}^{\substack{k=N \\ t=2}} \mathrm{Re}\left(\mathbf{\Phi}_t^{-1} \left(\mathbf{T}_k^t\right)^{-1} \mathbf{x}_k^t\, \mathbf{x}_k^{tH}\right),$$

$$\frac{\partial \log(\boldsymbol{\mathcal{L}}_1)}{\partial \mathbf{\Phi}_t^{-1}} = \sum_{\substack{k=1 \\ t=1}}^{\substack{k=N \\ t=2}} \mathbf{\Phi}_t - \sum_{\substack{k=1 \\ t=1}}^{\substack{k=N \\ t=2}} \mathbf{T}_{tk}^{-1} \mathbf{x}_k^t \mathbf{x}_k^{tH} \mathbf{T}_{tk}^{-1},$$

Letting the two previous equations be equal to $\mathbf{0}_{m\,p}$ leads to the following joint fixed point equations:

$$\begin{cases} \hat{\mathbf{T}}_k^t = \mathrm{Re}\left(\hat{\mathbf{\Phi}}_t^{-1} \left(\hat{\mathbf{T}}_k^t\right)^{-1} \mathbf{x}_k^t \mathbf{x}_k^{tH}\right), \\ \hat{\mathbf{\Phi}}_t = \frac{1}{N} \sum_{k=1}^{k=N} \left(\hat{\mathbf{T}}_k^t\right)^{-1} \mathbf{x}_k^t \mathbf{x}_k^{tH} \left(\hat{\mathbf{T}}_k^t\right)^{-1}. \end{cases} \quad (11)$$

Please note that, $\forall t \in \{1, 2\}$ and both hypotheses, $\mathbf{x}^{tH} \hat{\mathbf{T}}_t^{-1} \hat{\mathbf{\Phi}}_t^{-1} \hat{\mathbf{T}}_t^{-1} \mathbf{x}^t$ is a positive real scalar:

$$\begin{aligned} \mathbf{x}^{tH} \left(\hat{\mathbf{T}}_t \hat{\mathbf{\Phi}}_t \hat{\mathbf{T}}_t\right)^{-1} \mathbf{x}^t &= \mathrm{Re}\left(\mathrm{tr}\left(\left(\hat{\mathbf{T}}_t \hat{\mathbf{\Phi}}_t \hat{\mathbf{T}}_t\right)^{-1} \mathbf{x}^t \mathbf{x}^{tH}\right)\right), \\ &= \mathrm{tr}\left(\hat{\mathbf{T}}_t^{-1} \mathrm{Re}\left(\hat{\mathbf{\Phi}}_t^{-1} \hat{\mathbf{T}}_t^{-1} \mathbf{x}^t \mathbf{x}^{tH}\right)\right), \\ &= m\,p\,. \end{aligned}$$

Plugging the estimated parameters leads to the statistic $\hat{\Lambda}_B(\mathbf{x})$ given by (6).

REFERENCES

[1] K. Conradsen, A. A. Nielsen, J. Schou, and H. Skriver, "Change detection in polarimetric SAR data and the complex Wishart distribution," in *IGARSS 2001. Scanning the Present and Resolving the Future. Proceedings. IEEE 2001 International Geoscience and Remote Sensing Symposium (Cat. No.01CH37217)*, 2001, vol. 6, pp. 2628–2630 vol.6.

[2] L. M. Novak, "Coherent change detection for multi-polarization SAR," in *Conference Record of the Thirty-Ninth Asilomar Conference onSignals, Systems and Computers, 2005.*, Oct 2005, pp. 568–573.

[3] D. Ciuonzo, V. Carotenuto, and A. De Maio, "On multiple covariance equality testing with application to SAR change detection," *IEEE Transactions on Signal Processing*, vol. 65, no. 19, pp. 5078–5091, 2017.

[4] E. Ollila, J. Eriksson, and V. Koivunen, "Complex elliptically symmetric random variables - generation, characterization, and circularity tests," *IEEE Transactions on Signal Processing*, vol. 59, no. 1, pp. 58–69, Jan 2011.

[5] E. Ollila, D. E. Tyler, V. Koivunen, and H. V. Poor, "Complex elliptically symmetric distributions: Survey, new results and applications," *IEEE Transactions on Signal Processing*, vol. 60, no. 11, pp. 5597–5625, Nov 2012.

[6] A. Mian, G. Ginolhac, J.-P. Ovarlez Ovarlez, and A. M. Atto, "New robust statistics for change detection in time series of multivariate SAR images," *IEEE Transactions on Signal Processing*, vol. 67, no. 2, pp. 520–534, 2019.

[7] A. Mian, A. Collas, A. Breloy, G. Ginolhac, and J.-P. Ovarlez, "Robust low-rank change detection for multivariate SAR image time series," *IEEE Journal of Selected Topics in Applied Earth Observations and Remote Sensing*, vol. 13, pp. 3545–3556, 2020.

[8] O. Lerda, A. Mian, G. Ginolhac, J.-P. Ovarlez, and D. Charlot, "Robust detection for Mills cross sonar," *IEEE Journal of Oceanic Engineering*, 2024.

[9] A. Wiesel, "Unified framework to regularized covariance estimation in scaled Gaussian models," *IEEE Transactions on Signal Processing*, vol. 60, no. 1, pp. 29–38, 2011.

[10] K. Conradsen, A. A. Nielsen, and H. Skriver, "Determining the points of change in time series of polarimetric SAR data," *IEEE Transactions on Geoscience and Remote Sensing*, vol. 54, no. 5, pp. 3007–3024, May 2016.

[11] R. Baqué, P. Dreuillet, and H. Oriot, "SETHI: Review of 10 years of development and experimentation of the remote sensing platform," in *International Radar Conference*, 2019, pp. 1–5.

[12] K. B. Petersen and M. S. Pedersen, *The Matrix Cookbook*, Technical University of Denmark, nov 2012.